Materials Science & Engineering A 893 (2024) 146146

Contents lists available at ScienceDirect

Materials Science & Engineering A

journal homepage: www.elsevier.com/locate/msea

Dynamic recrystallisation in Inconel®718 at creep conditions

Kasyap Pradeep [a,b], Ricardo Henrique Buzolin [a,b], Maria Domankova [c], Flora Godor [d], Aleksandar Stanojevic [d], Maria Cecilia Poletti [a,b,*]

[a] Christian Doppler Laboratory for Design of High-Performance Alloys by Thermomechanical Processing, Graz, 8010, Austria
[b] Institute of Materials Science, Joining and Forming, Graz University of Technology, Graz, 8010, Austria
[c] Institute of Materials Science, Slovak University of Technology in Bratislava, Trnava, 91724, Slovakia
[d] Voestalpine Böhler Aerospace GmbH & Co KG, Kapfenberg, 8605, Austria

ARTICLE INFO

Keywords:
Creep
Nickel-based superalloy
Dislocation-based model
Dynamic recrystallisation
Mean-field model

ABSTRACT

Inconel®718 is a nickel-based superalloy primarily used in applications at high temperatures and loads. Its main characteristic is the high creep resistance due to a combination of microstructural features, mainly the presence of coherent intermetallic phases. Although the design of this type of alloy relies on controlling the distribution, nature and stability of the intermetallic phases, dislocations may play a determinant role on the creep resistance of nickel-based superalloys. This work investigates the creep resistance of Inconel®718 after two different heat treatments between 590 and 650 °C at 550 and 830 MPa stresses. After analysing the microstructure, we observe that dynamic recrystallisation happens at high temperatures and stresses, softening the material considerably. Therefore, we further develop mean-field models that predict the strain and microstructure evolutions during creep considering the size and fraction of precipitates, the dislocation densities, grain sizes and recrystallisation grade. Finally, we simulate the creep behaviour at different testing conditions and the initial microstructures and explore the robustness of the model beyond the measurement capabilities. The main conclusion is that an initial large amount of dislocations accelerates the nucleation and recrystallisation rates, decreasing the creep resistance of Inconel®718. In consequence, the material aged after forging presents lower creep resistance than the standard aged because of the larger initial dislocation density. On the contrary, the standard aged material undergo a strong reduction of the remaining dislocation density from forging during the solution treatment.

1. Introduction

Superalloys are the primary materials used in the hot zones of jet turbine engines, such as blades, vanes and combustion chambers, constituting over 50 % of the engine weight. Today, superalloys are used in other applications, such as rocket engines, steam turbine power plants, reciprocating engines, metal processing equipment, heat treating equipment, chemical and petrochemical plants, pollution control equipment, coal gasification and liquefaction systems, as well as medical applications [1–5].

Inconel®718 nickel-based superalloy is well-known for its high mechanical and creep resistances. It presents high fatigue resistance at high temperatures and is suitable for corrosive environments [6]. The most prominent feature that makes Inconel®718 attractive for its best mechanical properties is the presence of different precipitates [7]. The alloy has four distinct phases: the FCC matrix called γ and the precipitates γ′, γ′′ and δ. The γ′ phase is $Ni_3(Al,Ti)$ with a cubic (L12) crystal structure. The γ" phase is Ni_3Nb with bct (D022) crystal structure. The δ phase is Ni_3Nb with an orthorhombic (D0a) crystal structure [8,9]. The first two precipitates are responsible for the hardening effect, while the δ phase can be used to control the grain size, thus improving the hardness and ductility [10]. Solutes and precipitates reduce the mobility of dislocations and boundaries. The most well-known temperature-time transformation (TTT) diagram of Inconel®718 [11] shows that precipitates form below 930 °C during soaking. This precipitation accelerates during the annealing treatment after applying a plastic deformation [12]. Plastic deformation applied during the forging processes occurs above the solvus of the δ phase, meaning between 990 and 1020 °C [13]. Other works [14,15] concluded that the δ phase partially dissolves and breaks during deformation.

Creep is the consequence of the cross-slip and climb of perfect dislocations within the matrix, requiring partial dislocations recombining into perfect dislocations [16]. At high temperatures ($T > 0.5T_m$) that correspond to most of the service temperatures of superalloys, bulk

* Corresponding author. Christian Doppler Laboratory for Design of High-Performance Alloys by Thermomechanical Processing, Graz, 8010, Austria.
E-mail address: cecilia.poletti@tugraz.at (M.C. Poletti).

https://doi.org/10.1016/j.msea.2024.146146
Received 17 October 2023; Received in revised form 4 January 2024; Accepted 18 January 2024
Available online 19 January 2024

Table 1
Chemical composition of the studied Inconel®718.

Condition	Elemental composition (wt.%)										
	Ni	Cr	Fe	Mo	Al	Co	Si	Nb	C	Mn	Ti
SA	Bal.	17.96	17.12	2.97	0.51	0.38	0.07	5.42	0.024	0.09	0.98
DA	Bal.	17.92	17.18	2.99	0.56	0.27	0.07	5.42	0.021	0.08	1.02

self-diffusion is the dominant rate-controlling mechanism of the dislocation climb [17–19]. For moderate and low stacking fault energy materials, such as Inconel®718, plastic deformation also produces stacking faults or micro-twins [17,20]. The value of the stacking fault energy affects the recombination of the stacking faults (partial dislocations) into perfect dislocations [21]. Inconel®718 is also characterized by its low stacking fault energy. Therefore, it undergoes discontinuous dynamic recrystallisation (dDRX) [1–3] because the dislocations tend more to dissociate in partial dislocations than to annihilate and rearrange by dynamic recovery [4]. Inconel®718 form twins type $\sum 3$ during the recrystallisation [5,6]. Although the dynamic recrystallisation (DRX) reduces considerably the stored energy during forging [7,8], it may soften the material during creep. Some less literature on creep of Inconel®718 pay attention to the formation, movement, and annihilation of dislocations [22], but there is no reference about recrystallisation during service in the creep regime. Mostly, the minimum creep rate is just correlated to stress and temperature using phenomenological approaches [20,23].

Most physical creep models developed for Ni-based superalloys derive from Dyson's model [24]. Dyson's model considers the microstructure formed by channels between precipitates where the dislocation glides. The dislocations can glide and climb with a rate of production considering the interparticle distance and phase fraction of precipitates. Therefore, the climbing of dislocations dominates the creep strain rate. Since the dislocation climbs the precipitates, the model is referred to as the climb-glide bypass model [25]. Many groups further developed Dyson's model, for example, for single-crystal superalloys [26] and several polycrystal alloys with medium to high precipitate fractions [27]. In this last, a simultaneous strengthening of dislocations, carbides and γ' accounts for the interaction between dislocations and precipitates.

Most models summarise the dislocation climb and Orowan mechanism into a phenomenological precipitate backstress equation, such as the model developed by Coakley et al. [28]. A similar modelling approach developed for a C263 alloy [29] assumed the gliding dislocation density rate was zero at the steady-state creep. The analytical model developed by Li et al. [30] describes the influence of the γ' precipitates and carbides on the residual creep lifetime in a cast K417 Ni-based superalloy. Similarly, Kim et al. [31] modified the Dyson's approach to correlate the minimum creep rate to the precipitate size and fraction, channel width, grain size and stacking fault energy.

In sum, Dyson's models assume that the creep rate's controlling factor is the climb of dislocations over the precipitates due to trapping. However, they do not consider dynamic and static recovery phenomena for annihilating these dislocations. This work aims to describe the interaction of dislocations with boundaries and precipitates to determine the creep strain in a unified approach. We use the concepts of dislocation density-based creep model based on Ghoniem et al. [32], Yadav et al. [33], and Riedlsperger et al. [34,35] to elucidate the role of the different dislocation-microstructure features interactions on the primary and secondary creep regimes.

2. Materials and experimental methods

2.1. Material

The Inconel®718 studied in this work has the chemical composition shown in Table 1. The chemical composition was determined by spark spectroscopy. The material was provided in the forged condition and after 1) direct ageing (DA) and 2) standard ageing (SA). Table 2 shows the details of the heat treatments to obtain DA and SA conditions. The material in the DA condition represents one step less in the processing route, seeking for simplification of the process and less energy consumption.

Table 2
Heat treatments of Inconel®718 after forging.

Heat treatment	Temperature/time
Direct ageing	720 °C 8 h/free cooling Cooled up to 620 °C for 2 h 620 °C 8 h/air cooling
Standard ageing	980 °C 2 h/free cooling 720 °C 8 h/free cooling Cooled up to 620 °C for 2 h 620 °C 8 h/air cooling

Fig. 1 shows the microstructures of the as-received material after a,b) direct ageing (DA) and c,d) standard ageing (SA). Carbides e) and δ-phase f) are present in both conditions. The density of geometric necessary dislocations (GND) obtained by electron backscattered diffraction (EBSD) measurements (g) is larger for DA conditions than for SA due to the lower temperature treatment after hot forging. For the local misorientations calculated in kernel average misorientation (KAM) maps, see section 2.2.

2.2. Metallography

The as-received and crept samples were hot embedded, ground using SiC paper, and polished using metallographic oxide polishing suspension (OP–S) for microstructural investigation. We obtained secondary and backscattered electron (SE and BSE) scanning electron microscope (SEM) images using a Tescan Mira3 SEM. We performed electron back scattered diffraction (EBSD) measurements on areas of $(400\ \mu m)^2$ and $(80\ \mu m)^2$ using a step size of 0.5 μm and 0.15 μm, respectively, and using an Hikari camera. We standardized the confidence index considering the a grain with a minimum size of 2 points and a tolerance angle of 15° and cleaned the data points with a confidence index lower than 0.3 with the OIM Analysis® 8.6 software. Finally, we obtained the grain orientation spread (GOS) maps and the fractions of low-angle grain boundaries (LAGB), coincidence site lattice (CSL) and high-angle grain boundaries (HAGB). The KAM calculated for the fifth neighbour served for the calculation of the geometrically necessary dislocation (GND) density for the slip system $(111)<1\ \bar{1}\ 0>$ for a burger vector of 0.252 nm.

2.3. Precipitation state

Table 2 summarizes the heat treatments (DA and SA) of the analysed Inconel®718. After these treatments, we obtained two different precipitation states, as discussed in another publication [36]. The main characteristic is that γ' and γ'' present in the DA and SA materials, have different coarsening kinetics (see Table A3 in Appendix). The size of precipitates in the DA condition is more thermally stable. We used the approach proposed in Ref. [36] to simulate the precipitation kinetics using MatCalc© with the commercial Nickel database. All the necessary parameters for the calculation, such as temperature, strain and strain

Table 3
Mean-field model modified from Ghoniem et al. [32], Yadav et al. [33] and Riedlsperger et al. [34,35]. 'AR' stands for the deformed matrix, and 'DRX' for the recrystallized material.

Constitutive equations		Source
$\sigma = \sigma_{sr_x} + \sigma_{lr_x};\ x : AR, DRX$	Equation 1	[32]
$\sigma_{lr_x} = \alpha M G b \sqrt{\rho_{i_x} + \rho_{m_x}};\ x : AR, DRX$	Equation 2	[42]
Plastic strain rate		
$\dot{\varepsilon} = \frac{(1 - X_{DRX}) b \rho_{m_{AR}} v_{g_{AR}}}{M} + \frac{X_{DRX} b \rho_{m_{DRX}} v_{g_{DRX}}}{M}$	Equation 3	Orowan relationship
Dislocation velocities		
$v_{g_x} = a_g\ exp\left(-\frac{Q_{glide}}{k_B T}\right) exp\left(-\frac{\sigma_{lr_x} V_{act}}{k_B T}\right) sinh\left(\frac{\sigma V_{act}}{K_B T}\right);\ x : AR, DRX$	Equation 4	[34]
$v_{c_x} = v_{c_{d_x}} + v_{c_{p_x}};\ x : AR, DRX$	Equation 5	[32]
$v_{c_{d_x}} = \frac{\eta D_s \frac{G}{(1-\nu)} \Omega \sqrt{\rho_{i_x} + \rho_{m_x}}}{k_B T \left(1 - \eta\, ln\left(\frac{(1+\nu) G \Omega}{6\pi(1-\nu) k_B T} \sqrt{\rho_{i_x} + \rho_{m_x}}\right)\right)};\ x : AR, DRX$	Equation 6	[32]
$v_{c_{p_x}} = \frac{2\pi D_p \sigma_{th_x} \Omega b}{k_B T \left(a_{Ni}\ exp\left(\frac{W_{jog}}{2 k_B T}\right)\right)^2};\ x : AR, DRX$	Equation 7	[32]
Precipitate coarsening		
$r_p = \left(r_{p,0} + k_{p0}\ exp\left(\frac{Q_p}{RT}\right) \bullet t\right)^{1/3}$	Equation 8	[43]
Dislocation rate equations		
$\frac{d\rho_{m_{AR}}}{dt} = \frac{\rho_{m_{AR}} v_{g_{AR}}}{\lambda_{\rho_{AR}}} - \frac{\rho_{m_{AR}} v_{g_{AR}}}{\Phi_{AR}} - 8\rho_{m_{AR}} v_{c_{AR}} \sqrt{\rho_{m_{AR}} + \rho_{i_{AR}}} - \delta_{DRV} \rho_{m_{AR}} (\rho_{m_{AR}} + \rho_{i_{AR}}) v_{g_{AR}}$	Equation 9	[32]
$\frac{d\rho_{i_{AR}}}{dt} = \frac{\rho_{m_{AR}} v_{g_{AR}}}{\Phi_{AR}} - 8\rho_{i_{AR}} v_{c_{AR}} \sqrt{\rho_{m_{AR}} + \rho_{i_{AR}}} - \delta_{DRV} \rho_{m_{AR}} \rho_{i_{AR}}$	Equation 10	[32]
The rate equation for dynamic recrystallisation		
$\frac{dN_{DRX}}{dt} = \frac{N_0\ exp\left(-\frac{Q_{DRX}}{RT}\right)}{\Phi}$	Equation 11	Modified from [43]
$\frac{d\Phi_{DRX}}{dt} = v_{DRX} + \frac{dN_{DRX}/dt}{N_{DRX}} (\varphi_{cell} - \Phi_{DRX})$	Equation 12	Modified from [44]
Auxiliary variables related to the dislocation model		
$\lambda_{ss} = \sqrt{\frac{ln(3)}{\pi n_{eq}} + (2r_{eq})^2} - 2r_{eq}$	Equation 13	[45]
$r_{eq} = \sqrt{\frac{2}{3} \bullet \frac{\sum_i n_{v,i} \bullet r_{p,i}^2}{\sum_i n_{v,i} \bullet r_{p,i}}}$	Equation 14	[45]
$n_{eq} = \sum_i n_{v,i} \bullet 2r_i$	Equation 15	[45]
$f_{eq} = \frac{4\pi r_{eq}^3 \sum_i n_{v,i}}{3}$	Equation 16	[45]
$\lambda_\rho = \frac{1}{\left(\sqrt{\rho_m + \rho_i} + \frac{f_{prec}}{\lambda_{ss}} + \frac{1}{\Phi}\right)}$	Equation 17	[43]
Auxiliary variables related to the recrystallisation model		
$\varphi_{cell} = \frac{1}{\left(f_{cell1} \sqrt{\rho_m + \rho_i} + \frac{f_{cell2}}{\lambda_{ss}} + \frac{1}{\Phi}\right)}$	Equation 18	This work
$E_{DRX} = \frac{Gb^2(\rho_m + \rho_i)}{2} - 2\pi \left(\sum_i r_{p,i}^2 n_{v,i}\right) \frac{Gb^2 \Phi}{3}$	Equation 19	[43]
$v_{DRX} = M_{HAGB} E_{DRX}$	Equation 20	[43]
$M_{HAGB} = \frac{b t_{HAGB}}{k_B T} exp\left(-\frac{Q_{HAGB}}{RT}\right)$	Equation 21	[43]
$X_{DRX} = 1 - exp\left(-\frac{4\pi N_{DRX} (\Phi_{DRX})^3}{3}\right)$	Equation 22	Adapted from JMAK approach
Auxiliary variables without a role in rate equations		
$\Phi_{av} = \frac{\Phi_{DRX} \Phi}{X_{DRX} \Phi + (1 - X_{DRX}) \Phi_{DRX}}$	Equation 23	[46]

rate as a function of time, were provided from FEM simulations of the thermomechanical process of the delivered parts.

We simulated the precipitation kinetics of the alloy with an initial average grain size of ASTM 7.5 at forging at 980 °C, followed by water quenching and a two-step ageing DA or SA, according to Table 2. Finally, we determined the coarsening of the precipitates during the 600 h of creep.

2.4. Creep testing

The creep samples have DIN EN ISO 204 M16 standard dimensions with a total length of 90 mm, a gauge length of 32.5 mm and a diameter of 6.5 mm. We performed creep tests according to the ASTM E139 for 600 h at three different temperatures, 593, 620 and 650 °C and three different loads, 552, 662 and 827 MPa. The creep testing machine Mayes model mark II TC worked at a constant force. Inside the creep furnace we heated each sample for 6 h to achieve a constant temperature along their whole length, meaning that the gauge and head are at the same temperature. We loaded the sample in tension and measured their elongation using a couple of Linear Variable Differential Transformers (LVDT) for high temperatures. We obtained an average strain value out of the two displacement recordings. Three K–type thermocouples on the sample's bottom, middle (control) and top parts measured the specimen's actual temperature. The detected variation of temperature during the test was below 1 %.

3. Mean-field model

The concepts of dislocation density reactions proposed by Ghoniem et al. [32] and further developed by Yadav et al. [33] and Riedlsperger et al. [34,35] are the basis of the creep model developed here. Fig. 2 shows the modelling approach schematically. The following sections describe the microstructure concept, constitutive equations, and rate equations.

3.1. Microstructure and auxiliary variables

The first step in the model's development is the microstructure's conception. The microstructural variables are the initial and recrystallized grain sizes (Φ and Φ_{DRX}, respectively), mobile (ρ_m) and immobile (ρ_i) dislocation densities, and the precipitates. The γ′ and γ" precipitates are within the grains, hindering the movement of dislocations, and the δ phase is located at the high-angle grain boundaries. Fig. 3 shows a schematical representation of the dislocations and precipitates for the DA and SA conditions.

Some auxiliary variables complementarily define the microstructure and they are: the average precipitate interspace (λ_{ss}, Equation 13), equivalent precipitate radius (r_{eq}, Equation 14), number density (n_{eq}, Equation 15) and fraction (f_{eq}, Equation 16), mean-free dislocation path (λ_ρ, Equation 17), and average grain size (Φ_{av}, Equation 23). The auxiliary variables related to the dynamic recrystallisation model consist of the mean cell size (φ_{cell}, Equation 18), the stored energy for dynamic recrystallisation (E_{DRX}, Equation 19), the velocity (v_{DRX}, Equation 20) and mobility (M_{HAGB}, Equation 21) of grain boundaries, as well as of the recrystallisation fraction (X_{DRX}, Equation 22). The cell size computes a harmonic average of the grain size (Φ), a fraction of the mean-free dislocation path (λ_ρ) and the precipitate inter-spacing (λ_{ss}). The stored energy is calculated as the energy of the dislocation lines minus by the precipitate Zener pinning.

3.2. Constitutive equations

The sum of short and long-range stresses yields the total or applied stress (σ, Equation 1). The short-range stress (σ_{sr}) is related to the lattice resistance to dislocation movement due to interaction with the lattice

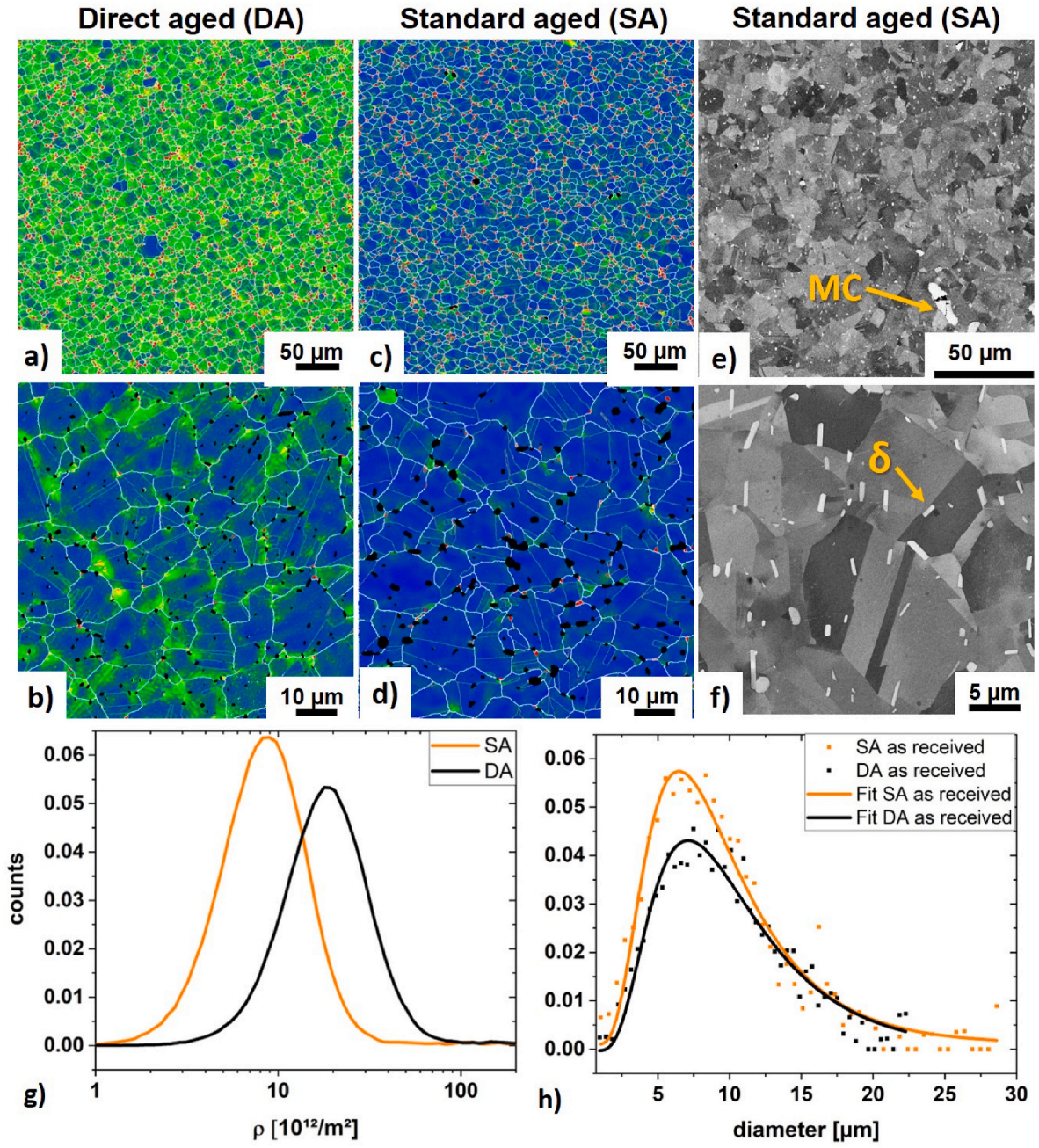

Fig. 1. As received condition of Inconel®718. Local misorientations are shown in KAM maps of a,b) direct aged condition and c,d) standard aged condition. Carbides e) and delta f) are present in both conditions. The GND density measured by EBSD (g) is larger for DA conditions than for SA. The grain size in both conditions is similar (h).

structure, such as phonons, substitutional and interstitial atoms. The long-range stress (σ_{lr}, Equation 2) is attributed to the strain field caused by dislocations. Equation 3 describes the plastic strain rate due to Orowan's relation for the material portion in the initial state ('AR') that underwent recrystallisation ('DRX').

3.3. Rate equations

The dislocation glide occurs with a glide velocity (v_g) given by Equation 4. The mean dislocation climb velocity (v_c, Equation 5) is the sum of climb velocity due to the annihilation of dipoles (v_{c_d}, Equation 6) with the dislocation climb velocity due to pipe diffusion (v_{c_p}, Equation 7). The high precipitate fraction in Nickel superalloys is associated with the high creep resistance due to the pinning of dislocations by the precipitates. For the dislocation climb controlling the creep rate [29,37–41] we used a similar glide velocity as proposed by Dyson's model [25], and for the dislocation glide we fitted the activation volume and energy. Therefore, our model proposes that the climb and glide of dislocations is responsible for the plastic deformation during creep.

The rate equations for dislocation densities are ordinary differential equations that describe the dislocation movement and dynamic recrystallisation. The dislocation reactions for the mobile and immobile dislocation densities are Equation 9 and Equation 10, respectively. The first term in Equation 9 describes the production rate of mobile dislocation due to the Frank-Read source. The second, third and fourth terms represent the consumption of mobile dislocations due to immobilization at grain boundaries, static recovery via climb, and dynamic recovery, respectively. Equation 10 gives the production of immobile dislocation

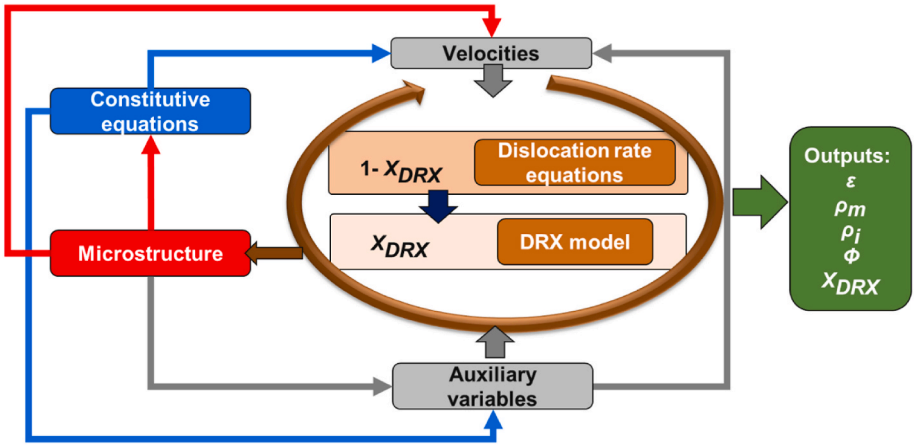

Fig. 2. Schematic structure of the mean-field model developed in this work.

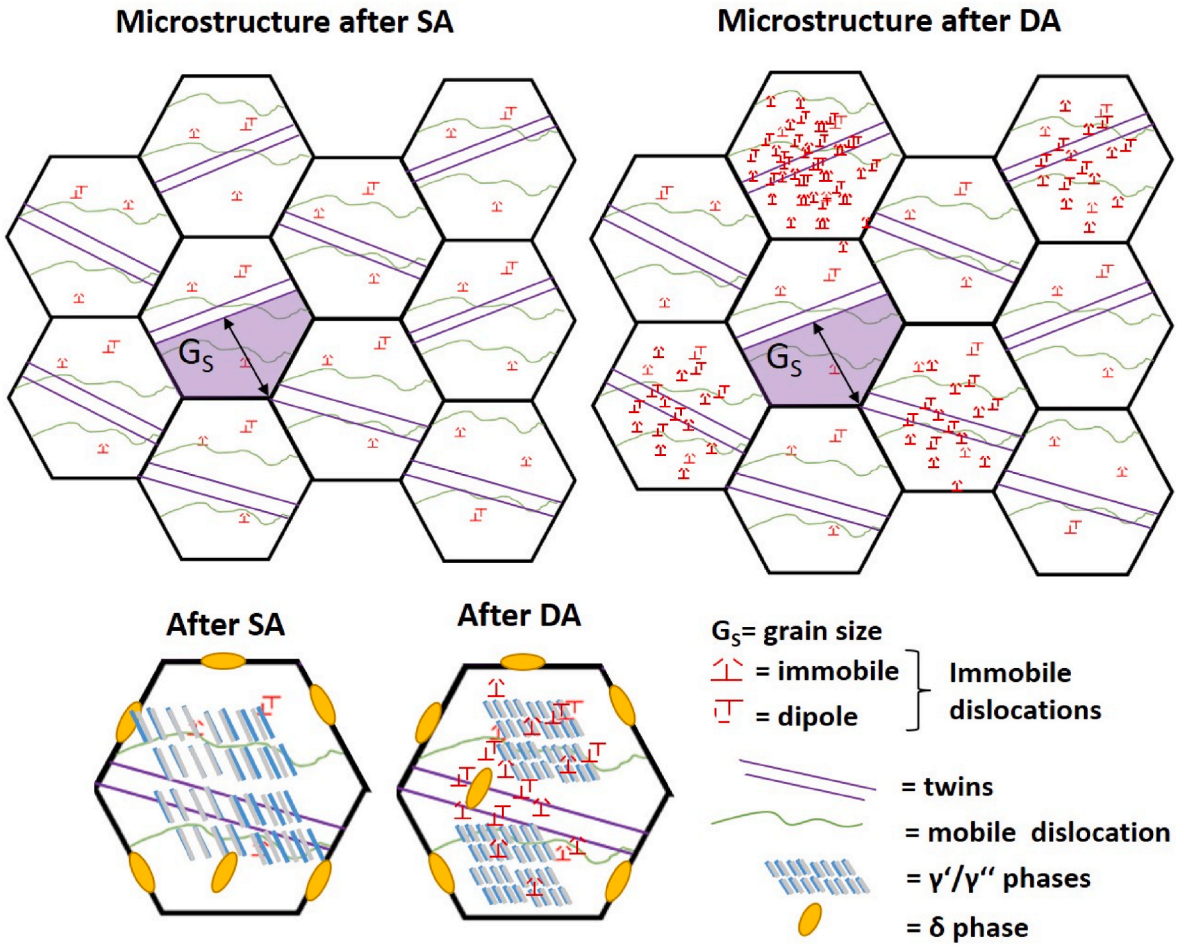

Fig. 3. Microstructure representation of the Inconel®718 after SA and DA heat treatments.

due to the immobilization of mobile dislocations at grain boundaries (first term) and the consumption of immobile dislocation due to static recovery (second term), and due to dynamic recovery (third term).

The dynamic recrystallisation model considered that the stored energy due to dislocations drives nucleation and growth of new grains during creep. We modelled the dynamic recrystallisation using nucleation (Equation 11) and growth laws (Equation 12). The nucleation law considers the effects of temperature and grain size, and the growth rate considers the velocity of the growing grains (first term in Equation 12) and the effect of the newly nucleated grains (second term in Equation 12). Finally, we obtained the total mobile and immobile dislocation densities (ρ_m and ρ_i) as weighted sums of the dislocations in the matrix (given by $\rho_{m_{AR}}$ and $\rho_{i_{AR}}$) and the dislocation density of the recrystallized material. The weighting factor is the recrystallisation grade. For the precipitate coarsening, we used a simple Ostwald-ripening law, Equation 8.(see. Table. 3)

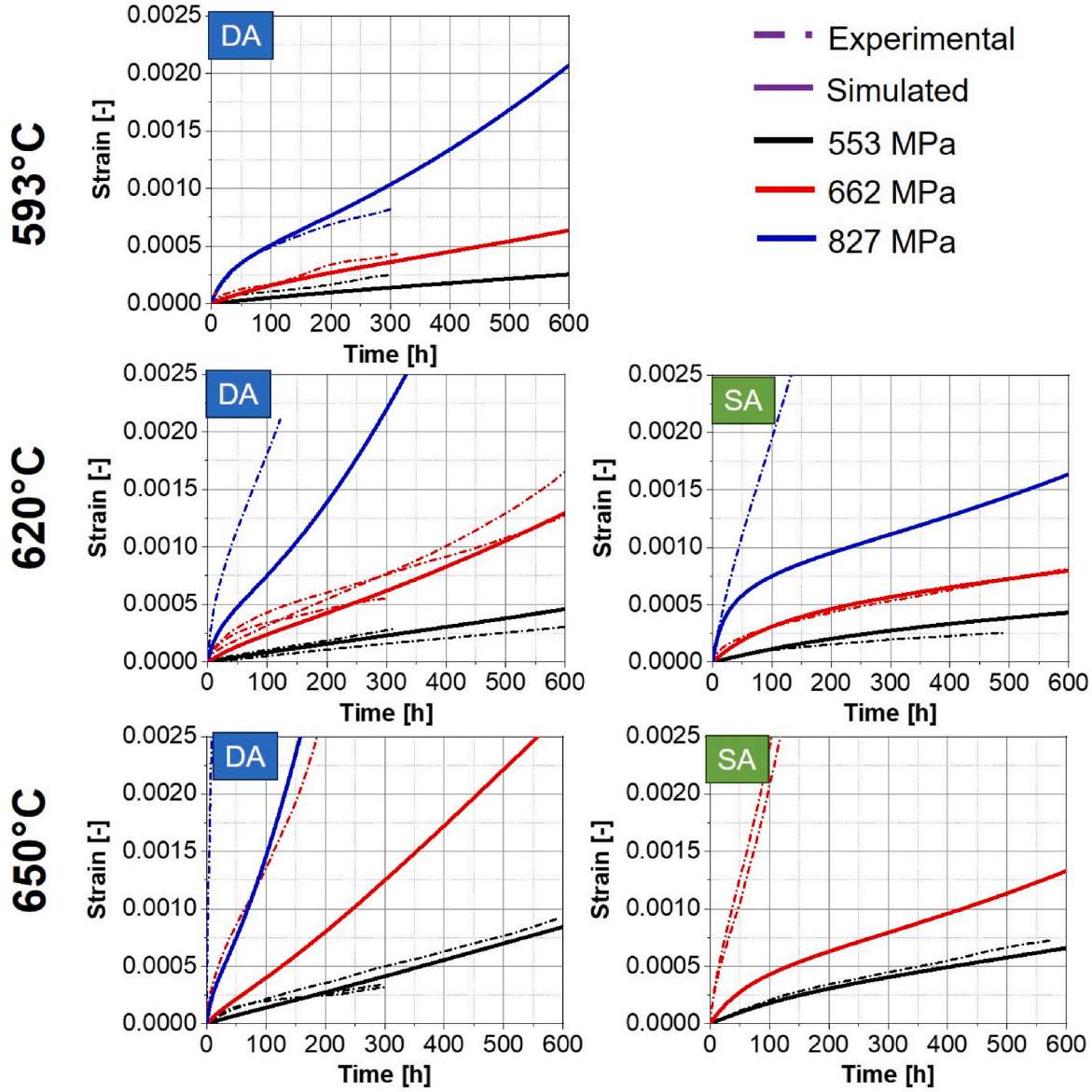

Fig. 4. Measured (M) and simulated (S) creep curves for the direct ageing (DA) and standard ageing (SA) samples. The simulations cover only primary and secondary creep stages.

4. Results

In this chapter, we present the modelled creep strain and the microstructure evolutions and validate the results with experimental data.

4.1. Creep strain curves

Fig. 4 shows the simulated (S) and measured (M) creep strain curves for the DA and SA samples. The simulations cover only primary and secondary creep stages. In general, we observed typical strain dependency on temperature and stresses: the higher the temperature and the higher the stresses, the larger the creep strains are. We compared the creep strain at 650 °C and 662 MPa obtained in this work with Inconel®718 [47–49] and found that we obtained a lower creep strain than reported by Kuo et al. [47] and a higher strain than that measured by Yeh et al. [49] and Zhang et al. [48] at slightly higher stresses. Finally, we observed that the creep strain in the secondary stage is slightly higher for the DA than for the SA condition, see Fig. 4. Although the coarsening kinetics of precipitates in DA is slower (see kinetic coefficients in Table A3 in Appendix) than in the SA condition, the experimental curves show faster softening in the DA condition. Therefore, the softening cannot be a consequence of the solely particle coarsening, and other microstructural feature must govern the creep resistance of Inconel®718 in the tested range of temperature and stresses.

The developed mean-field physical-based model can simulate the microstructure and creep strain at given conditions of temperature, applied stress and initial condition of the material. Fig. 4 shows that the higher the temperature, the higher the creep strain for a given time due to a) higher glide velocity (Equation 3) and b) faster recrystallisation. The faster recrystallisation leads to higher glide velocities. The applied stress also increases the creep rate because a) the glide velocity increases with the applied stress (Equation 4), and b) higher stresses lead to more mobile dislocations. Following the Orowan relationship (Equation 3), the creep strain rate increases due to the increment of the gliding velocity and the mobile dislocation density.

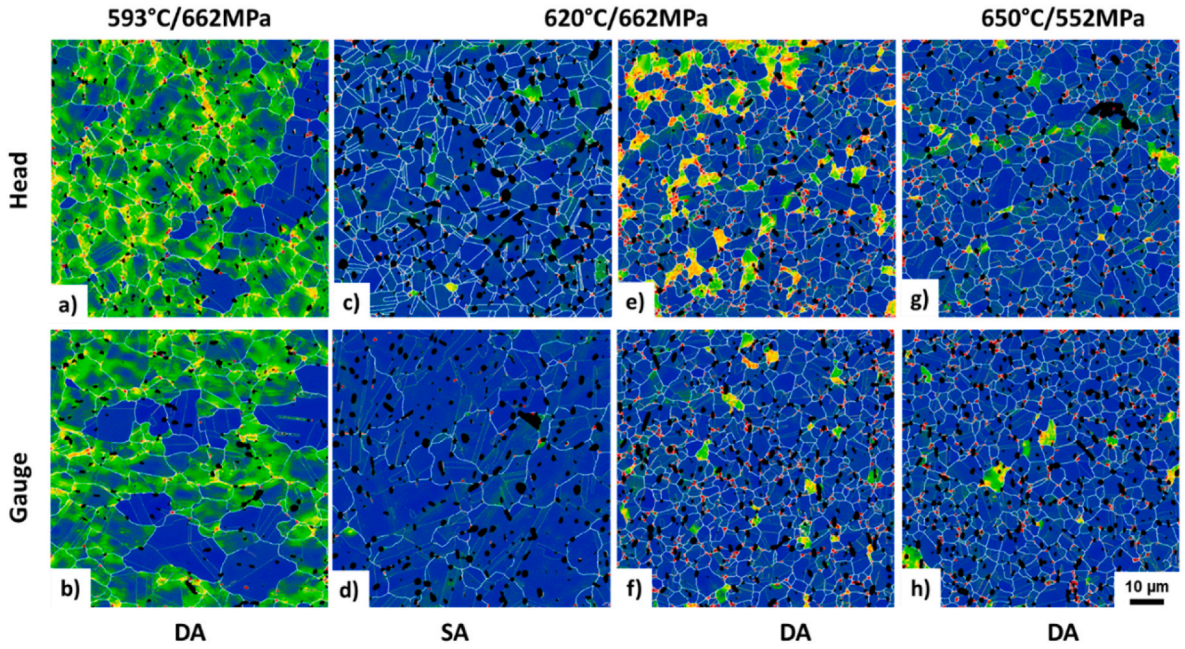

Fig. 5. Kernel average maps of non-deformed (head) and deformed (gauge) parts of the creep samples exposed to different creep temperatures and stresses.

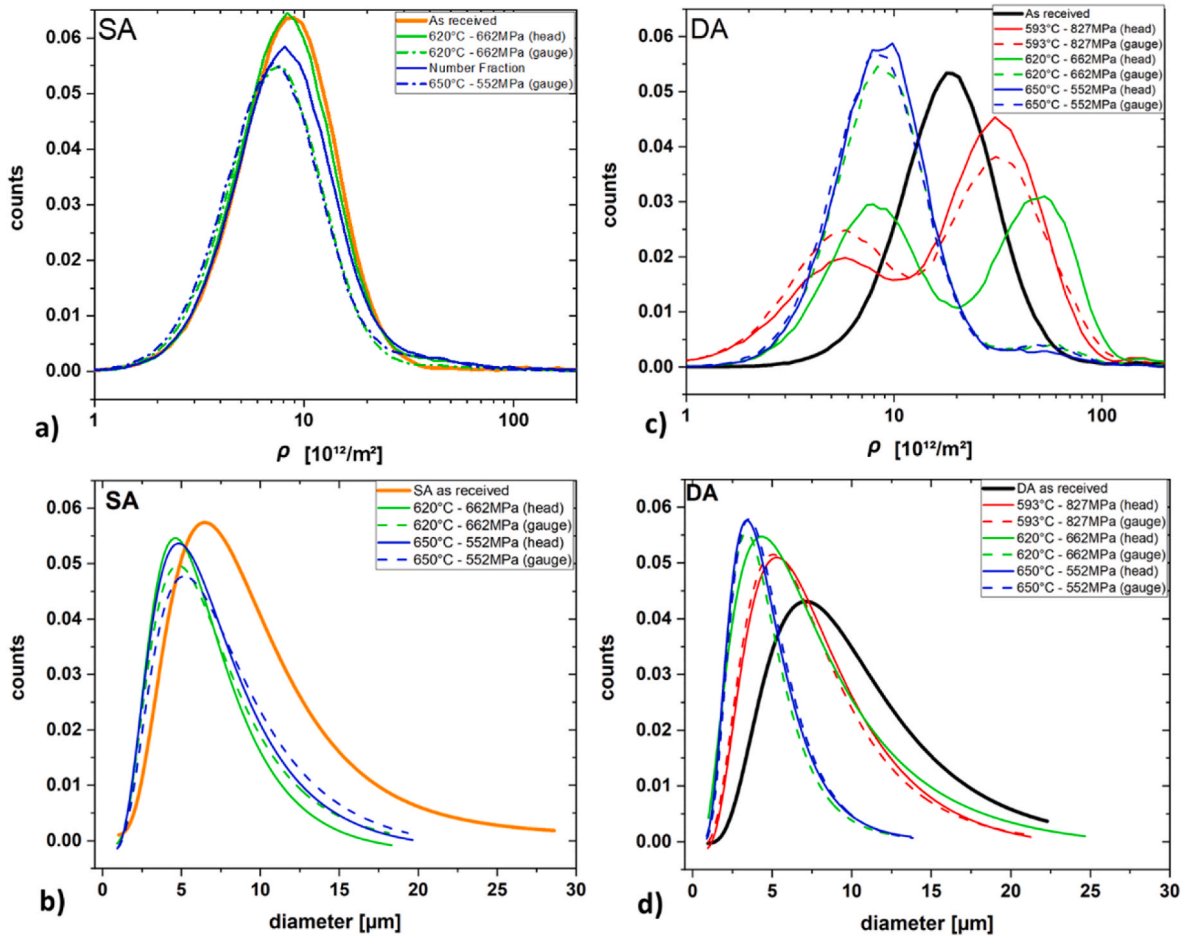

Fig. 6. Distributions obtained from the EBSD measurements of materials before and after creep in the a,b) SA and c,d) DA conditions of a,c) dislocation densities, and b,d) grain sizes.

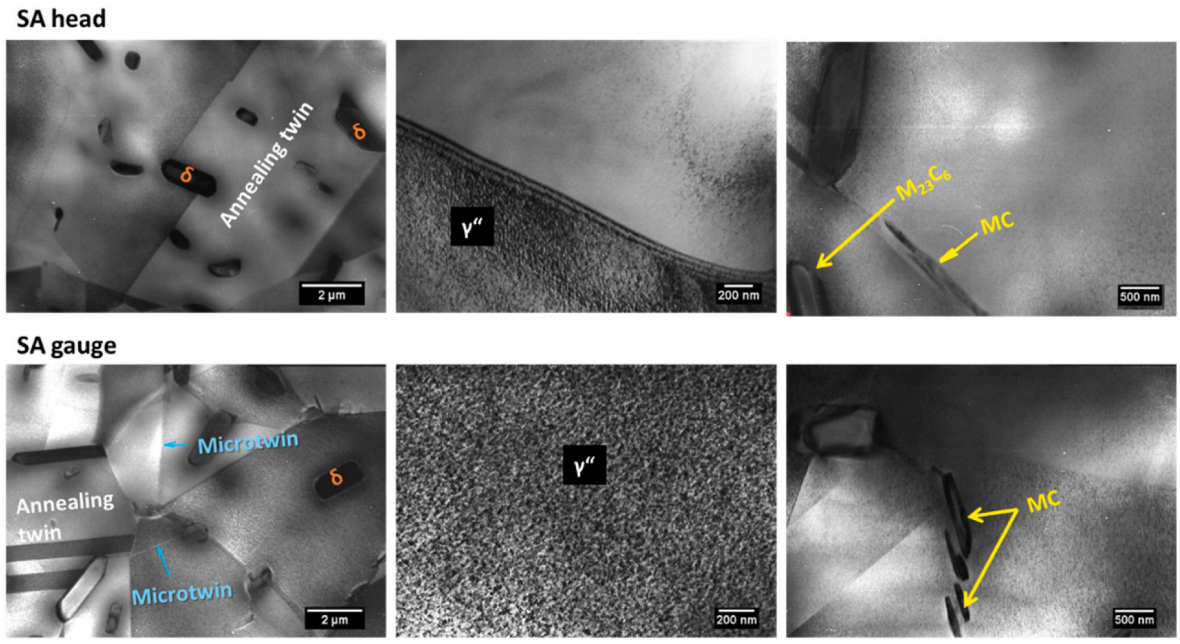

Fig. 7. TEM (bright field) micrographs showing phases and boundaries in the SA material after creep at 620 °C and 662 MPa for 600 h at the head and the gauge.

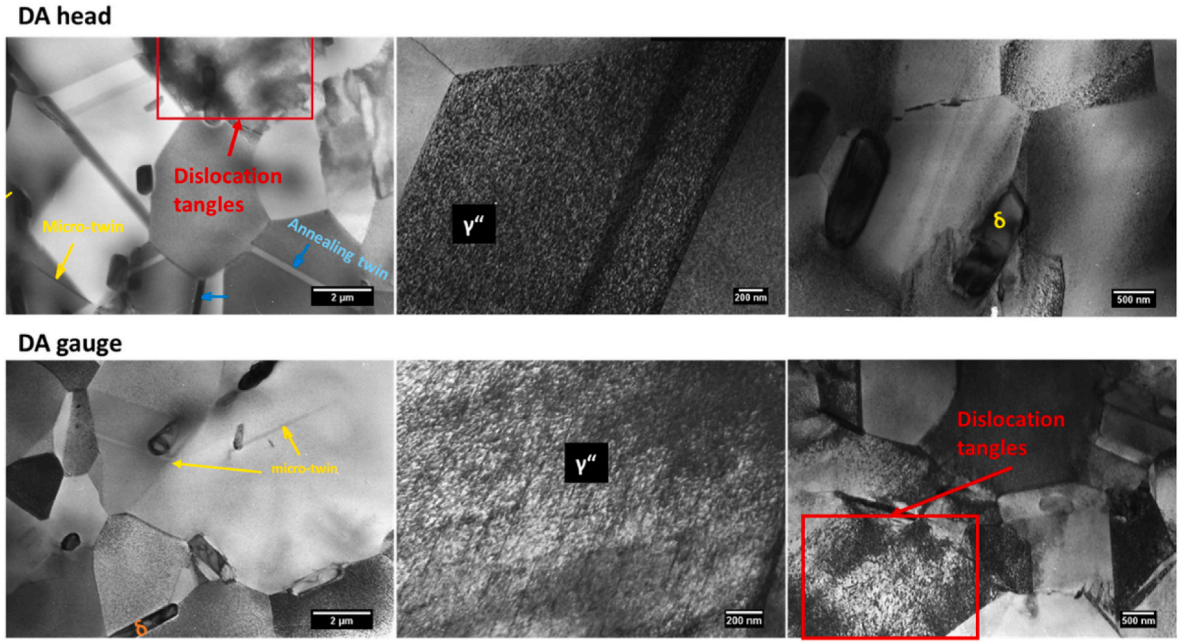

Fig. 8. TEM (bright field) micrographs showing the phases and boundaries in the DA material after creep at the head and the gauge.

4.2. Microstructure after creep

Fig. 5 shows the microstructures of crept samples in both DA and SA conditions. The head of the sample represents the materials exposed to the test temperature and negligible stresses. Here we observe that.

- The lower the temperature of the test, the higher the local misorientation, meaning the higher the dislocation density.
- Recrystallisation occurs during the creep test. The material in the DA condition also recrystallized statically at the head of the sample.
- The recrystallized grains have annealing twins.

Fig. 6 shows the distributions of the dislocation densities and grain sizes measured in samples before and after the exposure to temperature solely (head) and temperature and load (gauge). The GND density in the SA samples shows similar values before and after creep. In contrast, the grain size decreases after creep. Compared with the SA condition, we observed a higher dislocation density in the as-received sample in the DA condition. The bimodal distribution represents the deformed region from forging with a relatively high dislocation density and the recrystallized fraction with a low dislocation density. The gauge of DA samples shows higher intensity for lower dislocation density and refined grains than the head because of dynamic recrystallisation in the presence of stresses. The slight differences in the secondary creep regimes between the standard and direct aged materials are related to the extent of the recrystallisation that occurs faster for the DA material.

Figs. 7 and 8 show the results of TEM dark and bright field images after creep tests at 620 °C and 662 MPa for 600 h at the locations of the head and the gauge of SA and DA samples. The SA sample head and gauge (Fig. 7) present a polyhedral grain morphology and annealing

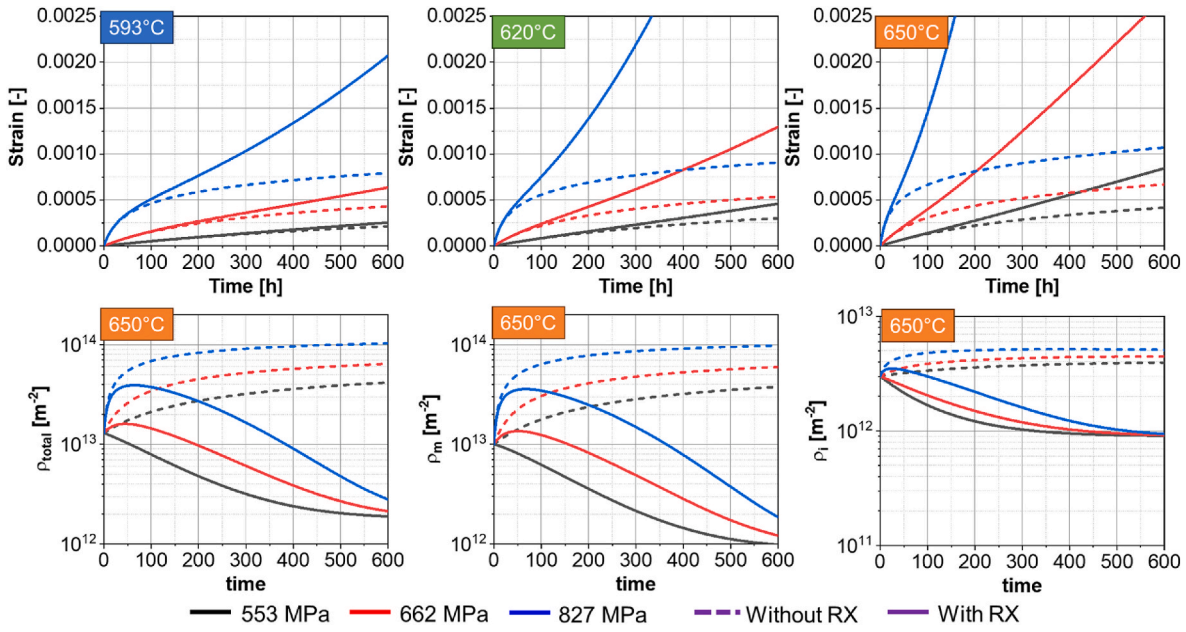

Fig. 9. Creep strain evolutions: a,b,c) with and without consideration of dynamic recrystallisation for a) 593 °C, b) 620 °C and c) 650 °C. Evolutions of the d) total (ρ_{total}), e) mobile (ρ_m) and f) immobile (ρ_i) dislocation densities.

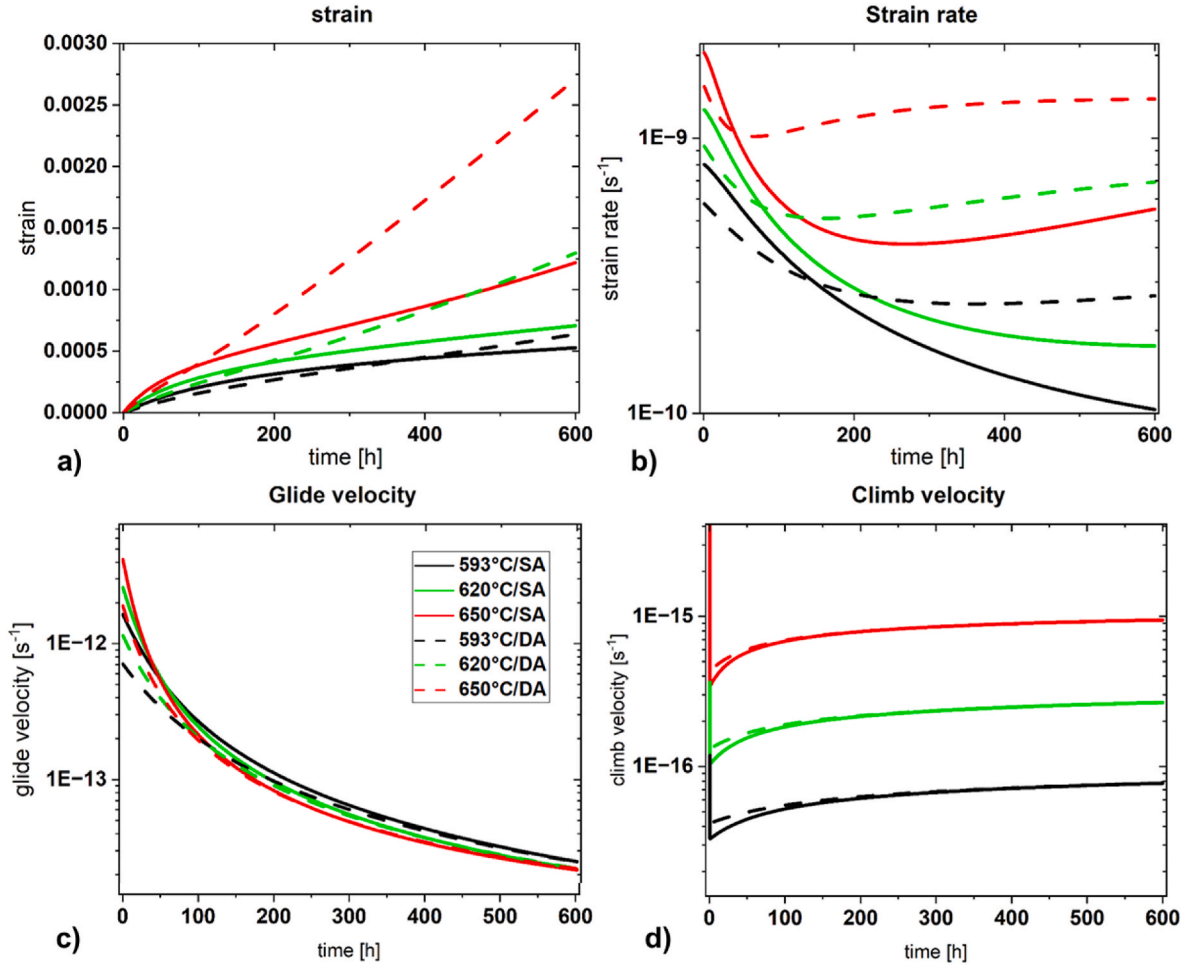

Fig. 10. Influence of the initial material's condition on the creep performance for a stress of 622 MPa. a) strain, b) strain rate, c) glide velocity and d) climb velocity.

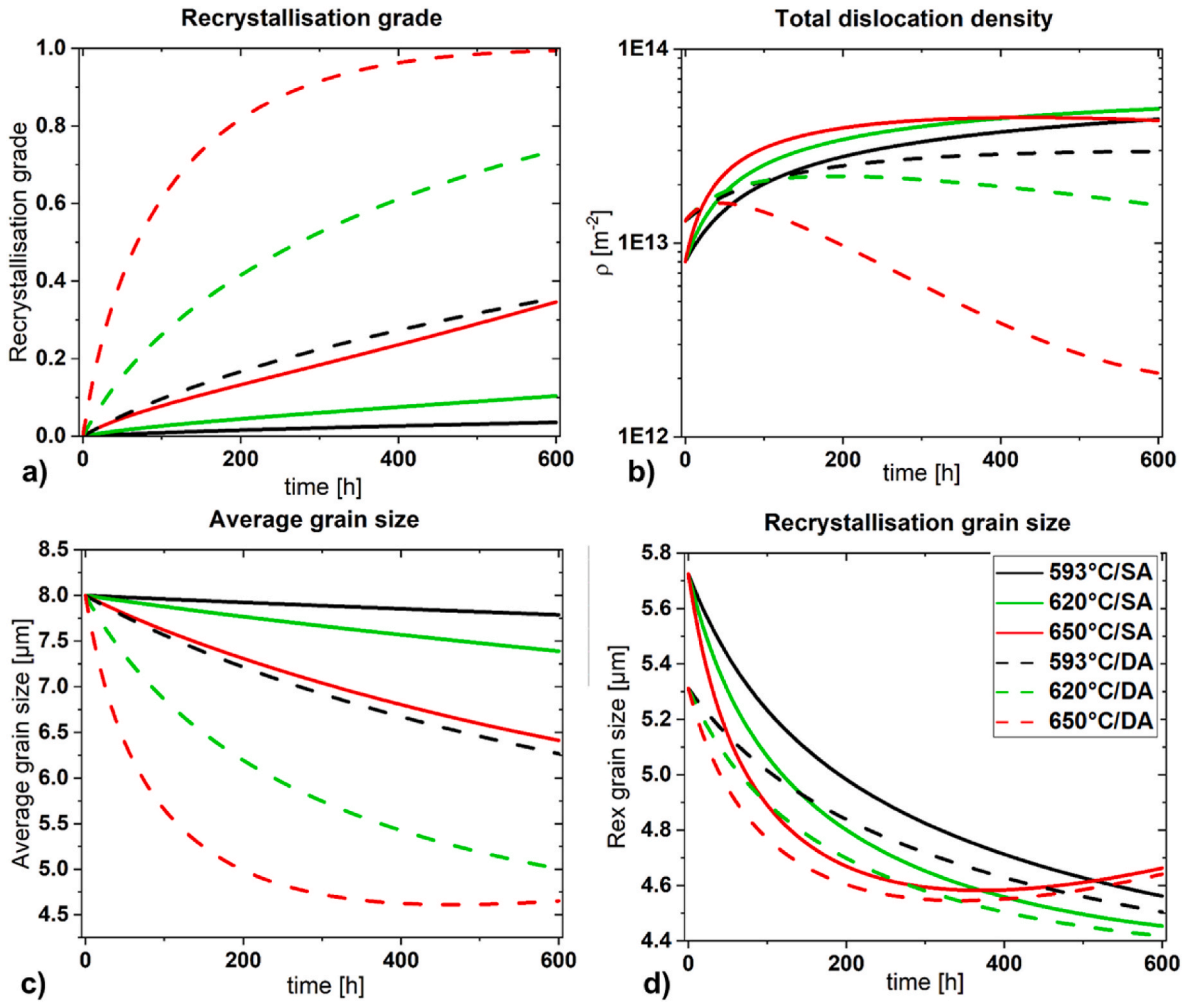

Fig. 11. Influence of the initial material's condition and the temperature on the microstructure for a stress of 622 MPa. a) recrystallisation grade, b) total dislocation density, c) average grain size d) recrystallized grain size.

twins. The samples in the DA condition show similar features to those in the SA condition (Fig. 8). Additionally, DA samples presented dislocation tangles and micro twins in the gauge and head from the forging process. In agreement with the EBSD measurements, we can conclude that the dislocations produced during hot forging could not annihilate after the age-hardening treatment and remained even after creep testing.

We identified particles with a needle or irregular shape as δ-phase (Ni_3Nb), carbides $M_{23}C_6$ and small quasi-globular particles as γ"-phase (Ni_3Nb) in all the samples. Smaller needle particles, sparely observed along the grain boundaries, were identified as MC carbide. Slightly larger γ"-phase particles were observed in the gauge compared to the head, indicating that deformation accelerated coarsening. We carried out indexation of the diffraction patterns to identify the phases.

5. Discussion

Dynamic (in the gauge) and static (in the head) recrystallisation occurs during testing due to the high temperatures and the remaining stored energy after forging. We modelled the dynamic recrystallisation using a simple nucleation and growth approach, Equation 11 and Equation 12 to account for this phenomenon. Table A1 gives the assumed values of initial dislocation density. Additionally, we assumed that the mobile and immobile dislocation density for the recrystallized grains is 9.10^{11} m^{-2}. A lower dislocation density means a higher glide velocity than in the deformed matrix. Since the increase in glide velocity predominates, the recrystallized material deforms during creep faster than the heat-treated matrix.

Fig. 9(a–c) shows the effect of recrystallisation on the predicted strain evolution for the three investigated temperatures. The calculated secondary creep rate is higher (solid lines in Fig. 9(a–c)) when considering dynamic recrystallisation. At lower temperatures, the kinetics of recrystallisation is slower. Thus, at lower temperatures, the predicted strain values in the secondary regime are similar for both models.

Fig. 9d, e, and f show the evolutions of the total, mobile and immobile dislocation densities for the hypothetical condition of no dynamic recrystallisation (dashed lines) and considering dynamic recrystallisation (solid lines). In agreement with the high KAM values in the crept and non-recrystallized areas in Fig. 5, both approaches predict hardening at the primary creep. The dislocation density decreases in the secondary creep stage only when considering recrystallisation. The dislocation density values decrease to $9 \bullet 10^{11}$ m^{-2} when 100 % of the microstructure recrystallises.

The initial microstructure of the material affects the creep strain rate. Therefore, the precipitation state, initial dislocation density, and grain size may accelerate or retard the creep rate. In this work, we analysed two materials with different initial dislocation densities and precipitation conditions; the initial grain size is for both materials the same. With the help of Fig. 10, we analyse the effect of the initial microstructure and temperature on the creep performance when loading at 662 MPa. The DA with higher dislocation density than SA creeps faster than SA (Fig. 10a and b). Analysing the velocity of dislocations, we could establish that the dislocations mostly climb since the glide velocity is

orders of magnitude smaller than the climb velocity. Furthermore, the dislocations will climb faster the higher the temperature due to the nature of the diffusional process. For the climb velocity, the initial microstructure plays a marginal role.

Therefore, asking what microstructural modification affects the creep rate is valid. Analysing the experimental results, we observe that the DA condition recrystallises faster than the SA condition, in agreement with Fig. 11a for all the creep temperatures at a load of 662 MPa. In the DA condition, the higher dislocation density must increase both the nucleation and the growth rates. The nucleation rate is higher mainly because the fitted pre-exponent N_0 is higher for DA than for SA. The growth rate is also faster in DA due to a higher stored energy in dislocations before creep (the first stage in Fig. 11b). The recrystallisation is then responsible for an abrupt decrease in the total dislocation density during creep, Fig. 11b, and the refining of the grains, Fig. 11c. Finally, the model allows calculating the recrystallized grain size as a function of the temperature and strain rate, as shown in Fig. 11d. We note here that the recrystallized grain size is larger with decreasing the temperature due to the lower strain rate.

6. Conclusions

We investigated the creep resistance of INCONEL® 718 for two different initial precipitate conditions: standard ageing and direct ageing. We developed a model to predict the strain and microstructure evolutions during primary and secondary creep that considers the precipitates (nature, size and amount), dislocation densities, and grain size. The obtained measurement and simulation results allow the following conclusions.

- Dynamic recrystallisation occurs during creep, especially at high temperatures and high stresses. The experimental evidence shows that the particles do not pin the boundaries.
- The developed mean-field model describes the intricate and complex interactions between dislocation reactions, glide and climb velocities, and long and short-range stresses. The model predicts the creep behaviour for differen initial microstructures.
- The differences in the creep regimes between the standard and direct ageing conditions are related to the extent of the recrystallisation, which occurs faster for the direct ageing material. The large dislocation density in the DA condition increases the rate of recrystallisation.
- At the tested conditions, the recrystallisation results in grain refinement. The grains are finer for higher creep temperatures.

CRediT authorship contribution statement

Kasyap Pradeep: Conceptualization, Data curation, Investigation, Methodology, Software, Validation, Visualization, Writing – original draft, Writing – review & editing. **Ricardo Henrique Buzolin:** Conceptualization, Data curation, Formal analysis, Investigation, Software, Validation, Visualization, Writing – original draft, Writing – review & editing. **Maria Domankova:** Data curation, Investigation, Methodology, Validation, Writing – review & editing, Visualization. **Flora Godor:** Data curation, Formal analysis, Software, Writing – review & editing. **Aleksandar Stanojevic:** Conceptualization, Data curation, Project administration, Writing – review & editing. **Maria Cecilia Poletti:** Conceptualization, Data curation, Formal analysis, Funding acquisition, Project administration, Resources, Supervision, Visualization, Writing – review & editing.

Declaration of generative AI and AI-assisted technologies in the writing process

During the preparation of this work the authors used Grammarly in order to improve the English writing. After using this tool/service, the authors reviewed and edited the content as needed and take full responsibility for the content of the publication.

Declaration of competing interest

The authors declare that they have no known competing financial interests or personal relationships that could have appeared to influence the work reported in this paper.

Data availability

Data will be made available on request.

Acknowledgements

The authors foster the Christian Doppler Laboratory for Design of High-Performance Alloys by Thermomechanical Processing with the support of the Christian Doppler Society. Open access funding by the Graz University of Technology is also acknowledged.

Appendix

Fig. A.1 shows the details of the creep sample.

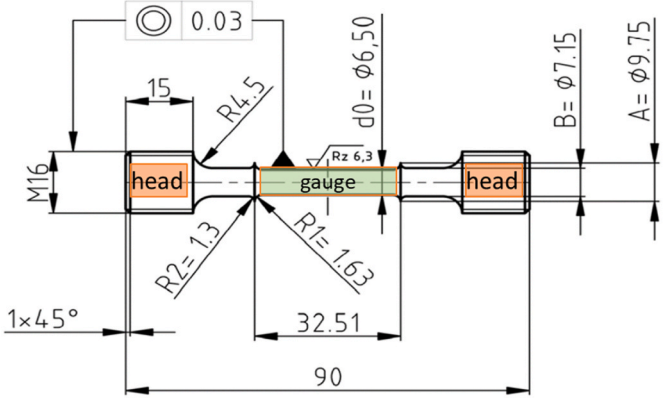

Fig. A.1. Detail of the creep sample.

The mobile and immobile dislocation densities, together with the grain size, describe microstructure before creep, and the values are given in Table A.1.

Table A.1
Initial microstructure parameters for the developed model.

Symbol	Meaning	Value		Unit
		Direct ageing	Standard ageing	
$\rho_{m_{AR0}}$	Initial mobile dislocation density (fitted)	$1{\cdot}10^{13}$	$6{\cdot}10^{12}$	m^{-2}
$\rho_{i_{M0}}$	Initial immobile dislocation density (fitted)	$3{\cdot}10^{12}$	$2{\cdot}10^{12}$	m^{-2}
Φ	Grain size (experimental)	8	8	μm

The parameters of the developed mean-field model are given in Table A.2.

Table A.2
Fitting parameters used for the mean-field model developed in this work.

Symbol	Meaning	Value	Unit
α	Taylor constant	0.15	–
a_g	Parameter for glide velocity	$6.50 \bullet 10^{-6}$	m/s
a_{Ni}	Cell parameter Nickel	$3.50 \bullet 10^{-10}$	m
b	Burgers vector	$2.54 \bullet 10^{-10}$	m
D_s	Self-diffusion	$9.2 \bullet 10^{-5} \exp\left(-\frac{Q_{sd}}{RT}\right)$	J/mol
D_p	Pipe-diffusion	$9.2 \bullet 10^{-4} \exp\left(-\frac{Q_{pd}}{RT}\right)$	J/mol
δ_{DRV}	Characteristic annihilation length for DRV	$20 \bullet b$	m
G	Shear modulus	$7.6 \bullet 10^{11}$	Pa
M	Taylor coefficient	3.1	–
η	Coefficient for transfer of defects into jogs	$1 \bullet 10^{-5}$	–
Q_{DRX}	Activation energy for nucleation during DRX	Q_{sd}	J/mol
Q_{glide}	Activation energy for dislocation glide	$0.52 \bullet Q_{sd}$	J/mol
Q_{sd}	Activation energy for self-diffusion	$2.78 \bullet 10^5$	J/mol
V_{act}	Activation energy for gliding	$18 \bullet \Omega$	m^3
ν	Poisson ratio	0.31	–
Ω	Atomic volume of Nickel	$7.99 \bullet 10^{-30}$	m^3
W_{jog}	Activation energy for jog formation in pipe diffusion	$0.52 \bullet Q_{sd}$	J/mol

The nucleation coefficient values adopted for the direct ageing and standard ageing condition are given in Table A.3.

Table A.3
Fitting parameters used for the mean-field model developed in this work related to the nucleation rate.

Nucleation coefficient	Direct ageing	Standard ageing	Unit
N_0	$1 \bullet 10^{21}$	$8 \bullet 10^{19}$	m/s

The parameters related to the precipitate state and its coarsening are given in Table A.4.

Table A.4
Fitting parameters used for the mean-field model developed in this work.

Symbol	Meaning	Value		Unit
		Direct ageing	Standard ageing	
$k_{p0,\gamma'}$	Ostwald ripening parameter for coarsening of γ'	$1.16 \bullet 10^{-14}$	$1.02 \bullet 10^{-15}$	m^3/s
$k_{p0,\gamma''}$	Ostwald ripening parameter for coarsening of γ''	$1.80 \bullet 10^{-7}$	$6.44 \bullet 10^{-13}$	m^3/s
$n_{v0,\gamma'}$	Initial mean volumetric number density of γ'	$4.76 \bullet 10^{22}$	$9.5 \bullet 10^{22}$	m^{-3}
$n_{v0,\gamma''}$	Initial mean volumetric number density of γ''	$3.98 \bullet 10^{22}$	$6.03 \bullet 10^{22}$	m^{-3}
$Q_{p,\gamma'}$	Activation energy for Ostwald ripening coarsening of γ'	$2.56 \bullet 10^6$	$2.37 \bullet 10^6$	J/mol
$Q_{p,\gamma''}$	Activation energy for Ostwald ripening coarsening of γ''	$3.76 \bullet 10^6$	$2.8 \bullet 10^6$	J/mol
$r_{0,\gamma'}$	Initial radius of γ'	$6.93 \bullet 10^{-9}$	$5.81 \bullet 10^{-9}$	m
$r_{0,\gamma''}$	Initial radius of γ''	$8.98 \bullet 10^{-9}$	$7.45 \bullet 10^{-9}$	m

References

[1] Roger C. Reed, The Superalloys: Fundamentals and Applications, Cambridge University Press, 2008, 2008.
[2] W.C.H. Chester, T. Sims, Norman S. Stoloff, Superalloys II: High-Temperature Materials for Aerospace and Industrial Power, 1987.
[3] A.P.B.T.-I. to, A.M. Mouritz (Eds.), 12 - Superalloys for Gas Turbine Engines, Woodhead Publishing, 2012, pp. 251–267, https://doi.org/10.1533/9780857095152.251.
[4] R.C. Reed, Roger C. Reed, The Superalloys: Fundamentals and Applications, Cambridge University Press, Cambridge, 2006, https://doi.org/10.1017/CBO9780511541285.
[5] R.E. Schafrik, D.D. Ward, J.R. Groh, Application of alloy 718 in GE aircraft engines: past, present and next five years, in: Superalloys 718, 625, 706 and *Various*

Derivatives (2001), TMS, 2001, pp. 1–11, https://doi.org/10.7449/2001/Superalloys_2001_1_11.
[6] E. Akca, A. Gursel, A review on superalloys and IN718 nickel-based INCONEL superalloy, Period. Eng. Nat. Sci. 1 (Jun) (2015), https://doi.org/10.21533/pen.v3i1.43.
[7] M.R. Ahmadi, E. Povoden-Karadeniz, L. Whitmore, M. Stockinger, A. Falahati, E. Kozeschnik, Yield strength prediction in Ni-base alloy 718Plus based on thermo-kinetic precipitation simulation, Mater. Sci. Eng., A 608 (Jul. 2014) 114–122, https://doi.org/10.1016/j.msea.2014.04.054.
[8] R. Cozar, A. Pineau, Morphology of γ' and γ" precipitates and thermal stability of inconel 718 type alloys, Metall. Trans. A 4 (1) (Jan. 1973) 47–59, https://doi.org/10.1007/BF02649604.
[9] M. Sundararaman, P. Mukhopadhyay, S. Banerjee, Some aspects of the precipitation of metastable intermetallic phases in INCONEL 718, Metall. Trans. A 23 (7) (Jul. 1992) 2015–2028, https://doi.org/10.1007/BF02647549.
[10] Y. Wang, W.Z.Z. Shao, L. Zhen, B.Y.Y. Zhang, Hot deformation behavior of delta-processed superalloy 718, Mater. Sci. Eng., A 528 (7–8) (Mar. 2011) 3218–3227, https://doi.org/10.1016/j.msea.2011.01.013.
[11] A. Oradei-Basile, J.F. Radavich, A current T-T-T diagram for wrought alloy 718, in: *Superalloys 718, 625 and Various Derivates*, the Minerals, Metals & Materials Society, 1991, pp. 325–335.
[12] L. Renhof, C. Krempaszky, E. Werner, M. Stockinger, Analysis of microstructural properties of in 718 after high speed forging, in: Proceedings of the International Symposium on Superalloys and Various Derivatives, Jan. 2005, https://doi.org/10.7449/2005/Superalloys_2005_261_270.
[13] D.Y. Cai, W.H. Zhang, P.L. Nie, W.C. Liu, M. Yao, Dissolution kinetics and behavior of δ phase in Inconel 718, Trans. Nonferrous Metals Soc. China 13 (Dec. 2003) 1338–1341.
[14] Y.C.C. Lin, et al., EBSD analysis of evolution of dynamic recrystallization grains and δ phase in a nickel-based superalloy during hot compressive deformation, Mater. Des. 97 (May 2016) 13–24, https://doi.org/10.1016/j.matdes.2016.02.052.
[15] P. Páramo-Kañetas, U. Özturk, J. Calvo, J.M. Cabrera, M. Guerrero-Mata, High-temperature deformation of delta-processed Inconel 718, J. Mater. Process. Technol. 255 (May 2018) 204–211, https://doi.org/10.1016/j.jmatprotec.2017.12.014.
[16] Madeleine Durand-Charre, The Microstructure of Superalloys, CRC Press, 1998, 1998.
[17] J.L. Peter, M. Anderson, John P. Hirth, Theory of Dislocations, Cambridge University Press, 2017, 2017.
[18] D. Hull, D.J. Bacon, Introduction to Dislocations, fifth ed., Butterworth-Heinemann, Oxford, 2011.
[19] European Creep Collaborative Committee, Creep and Fracture in High Temperature Components, DEStech Publications, Inc, 2005, 2005.
[20] F. de V.F. R.N. Nabarro, Physics of Creep and Creep-Resistant Alloys, CRC Press, 1995, p. 1995.
[21] M.N. Shetty, DISLOCATIONS AND MECHANICAL BEHAVIOUR OF MATERIALS, vol. 2013, PHI Learning Pvt. Ltd., 2013.
[22] B.W.R.W. Evans, Creep of Metals and Alloys, Institute of Metals, Metals Society, 1985.
[23] M.H. YuriEstrin, Creep properties of an oxide dispersion strengthened nickel-base alloy: the effect of grain orientation and grain aspect ratio, Elsevier 272 (1) (1999) 163–173.
[24] B.F. Dyson, Microstructure based creep constitutive model for precipitation strengthened alloys: theory and application, Mater. Sci. Technol. 25 (2) (Feb. 2009) 213–220, https://doi.org/10.1179/174328408X369348.
[25] B.F. Dyson, Microstructure based creep constitutive model for precipitation strengthened alloys: theory and application, Mater. Sci. Technol. 25 (2) (Feb. 2009) 213–220, https://doi.org/10.1179/174328408X369348.
[26] Z. Zhu, H. Basoalto, N. Warnken, R.C. Reed, A model for the creep deformation behaviour of nickel-based single crystal superalloys, Acta Mater. 60 (12) (2012) 4888–4900, https://doi.org/10.1016/j.actamat.2012.05.023.
[27] J. Haan, A. Bezold, C. Broeckmann, Interaction between particle precipitation and creep behavior in the NI-base Alloy 617B: microstructural observations and constitutive material model, Mater. Sci. Eng., A 640 (2015) 305–313, https://doi.org/10.1016/j.msea.2015.06.002.
[28] J. Coakley, D. Dye, H. Basoalto, Creep and creep modelling of a multimodal nickel-base superalloy, Acta Mater. 59 (3) (2011) 854–863, https://doi.org/10.1016/j.actamat.2010.08.035.
[29] A. Manonukul, F.P.E. Dunne, D. Knowles, Physically-based model for creep in nickel-base superalloy C263 both above and below the gamma solvus, Acta Mater. 50 (11) (2002) 2917–2931, https://doi.org/10.1016/S1359-6454(02)00119-2.
[30] S. Li, B. Wang, D. Shi, X. Yang, H. Qi, A physically based model for correlating the microstructural degradation and residual creep lifetime of a polycrystalline Ni-based superalloy, J. Alloys Compd. 783 (2019) 565–573, https://doi.org/10.1016/j.jallcom.2018.11.417.
[31] Y.-K. Kim, D. Kim, H.-K. Kim, C.-S. Oh, B.-J. Lee, An intermediate temperature creep model for Ni-based superalloys, Int. J. Plast. 79 (2016) 153–175, https://doi.org/10.1016/j.ijplas.2015.12.008.
[32] N.M. Ghoniem, J.R. Matthews, R.J. Amodeo, Dislocation model for creep in engineering materials, Res. Mech. 29 (3) (1990) 197–219.
[33] S.D. Yadav, B. Sonderegger, M. Stracey, C. Poletti, Modelling the creep behaviour of tempered martensitic steel based on a hybrid approach, Mater. Sci. Eng. 662 (2016), https://doi.org/10.1016/j.msea.2016.03.071.
[34] F. Riedlsperger, et al., Application of an advanced mean-field dislocation creep model to P91 for calculation of creep curves and time-to-rupture diagrams, Materialia 12 (2020) 100760, https://doi.org/10.1016/j.mtla.2020.100760.
[35] F. Riedlsperger, et al., Microstructural insights into creep of Ni-based alloy 617 at 700 °C provided by electron microscopy and modelling, Mater. Char. 198 (2023) 112720, https://doi.org/10.1016/j.matchar.2023.112720.
[36] A. Drexler, et al., Experimental and numerical investigations of the γ" and γ' precipitation kinetics in Alloy 718, Mater. Sci. Eng., A 723 (Apr. 2018) 314–323, https://doi.org/10.1016/j.msea.2018.03.013.
[37] Z. Zhu, H. Basoalto, N. Warnken, R.C. Reed, A model for the creep deformation behaviour of nickel-based single crystal superalloys, Acta Mater. 60 (12) (2012) 4888–4900, https://doi.org/10.1016/j.actamat.2012.05.023.
[38] J. Haan, A. Bezold, C. Broeckmann, Interaction between particle precipitation and creep behavior in the NI-base Alloy 617B: microstructural observations and constitutive material model, Mater. Sci. Eng., A 640 (2015) 305–313, https://doi.org/10.1016/j.msea.2015.06.002.
[39] J. Coakley, D. Dye, H. Basoalto, Creep and creep modelling of a multimodal nickel-base superalloy, Acta Mater. 59 (3) (2011) 854–863, https://doi.org/10.1016/j.actamat.2010.08.035.
[40] S. Li, B. Wang, D. Shi, X. Yang, H. Qi, A physically based model for correlating the microstructural degradation and residual creep lifetime of a polycrystalline Ni-based superalloy, J. Alloys Compd. 783 (2019) 565–573, https://doi.org/10.1016/j.jallcom.2018.11.417.
[41] Y.-K. Kim, D. Kim, H.-K. Kim, C.-S. Oh, B.-J. Lee, An intermediate temperature creep model for Ni-based superalloys, Int. J. Plast. 79 (2016) 153–175, https://doi.org/10.1016/j.ijplas.2015.12.008.
[42] R.J. McElroy, Z.C. Szkopiak, Dislocation–substructure–strengthening and mechanical–thermal treatment of metals, Int. Metall. Rev. 17 (1) (1972) 175–202, https://doi.org/10.1179/imtlr.1972.17.1.175.
[43] F.J. Humphreys, M. Hatherly, Recrystallization and Related Annealing Phenomena, Elsevier, 2004.
[44] A. Deschamps, Y. Brechet, Influence of predeformation and ageing of an Al–Zn–Mg alloy—II. Modeling of precipitation kinetics and yield stress, Acta Mater. 47 (1) (1998) 293–305, https://doi.org/10.1016/S1359-6454(98)00296-1.
[45] B. Sonderegger, E. Kozeschnik, Particle strengthening in fcc crystals with prolate and oblate precipitates, Scripta Mater. 66 (1) (2012) 52–55, https://doi.org/10.1016/j.scriptamat.2011.10.003.
[46] R.H.R.H. Buzolin, D. Canelo-Yubero, F. Warchomicka, M. Lasnik, A. Krumphals, M. C.M.C. Poletti, Refinement of the Ti-17 microstructure after hot deformation: coupled mesoscale model, Mater. Sci. Eng., A 800 (2021) 140268, https://doi.org/10.1016/j.msea.2020.140268.
[47] C.-M. Kuo, Y.-T. Yang, H.-Y. Bor, C.-N. Wei, C.-C. Tai, Aging effects on the microstructure and creep behavior of Inconel 718 superalloy, Mater. Sci. Eng., A 510 (511) (2009) 289–294, https://doi.org/10.1016/j.msea.2008.04.097.
[48] H. Zhang, C. Li, Q. Guo, Z. Ma, H. Li, Y. Liu, Improving creep resistance of nickel-based superalloy Inconel 718 by tailoring gamma double prime variants, Scripta Mater. 164 (2019) 66–70, https://doi.org/10.1016/j.scriptamat.2019.01.041.
[49] A.-C. Yeh, K.-W. Lu, C.-M. Kuo, H.-Y. Bor, C.-N. Wei, Effect of serrated grain boundaries on the creep property of Inconel 718 superalloy, Mater. Sci. Eng., A 530 (2011) 525–529, https://doi.org/10.1016/j.msea.2011.10.014.